Solid Electrolyte-Cathode Interface Dictates Reaction Heterogeneity and Anode Stability

Kaustubh G. Naik,[#] Debanjali Chatterjee,[#] and Partha P. Mukherjee[*]

School of Mechanical Engineering, Purdue University, West Lafayette, IN 47907, USA

[#]Contributed equally to this work.

[*]*Correspondence*: pmukherjee@purdue.edu

Abstract:

Solid-state batteries (SSBs) employing lithium metal anode are a promising candidate for next-generation energy storage systems, delivering higher power and energy densities. Interfacial instabilities due to non-uniform electrodeposition at the anode-solid electrolyte (SE) interface pose major constraints on the safety and endurance of SSBs. In this regard, non-uniform kinetic interactions at the anode-SE interface which are derived from cathode microstructural stochasticity can have significant impact on anode stability. In this work, we present a comprehensive insight into microstructural stochasticity-driven cathode-anode crosstalk and delineate the role of cathode architecture and SE separator design in dictating reaction heterogeneity at the anode-SE interface. We show that intrinsic and extrinsic parameters such as cathode loading, separator thickness, particles morphologies of active material (AM) and SE, and temperature can have significant impact on reaction heterogeneity at anode-SE interface and thus govern the anode stability. Tradeoff between energy density versus reaction heterogeneity while achieving higher cathode loading and thinner SE separators is highlighted and potential strategies to mitigate this problem are discussed. This work provides fundamental insights into cathode-anode crosstalk involving interfacial heterogeneities and enhancement in energy densities of SSBs via electrode engineering.

Keywords

solid-state batteries, cathode microstructure, cathode-solid electrolyte interface, anode-solid electrolyte interface, anode stability, architected cathode, reaction heterogeneity

1. Introduction:

Due to the ever-increasing demands of vehicle electrification, tremendous research efforts have been directed towards achieving high power and energy densities in energy storage systems[1-3]. As conventional lithium-ion batteries approach their theoretical limits in this aspect, incorporation of lithium metal anode appears to be an enticing choice due to its low electrochemical potential (-3.04 V vs. Standard Hydrogen Electrode), low material density (0.534 g cm^{-3}) and high theoretical capacity (3860 mAh g^{-1})[4-7]. In addition to the Li-metal anode being entirely electrochemically active, the metallic nature of lithium ensures negligible electron transport resistance. However, employing Li-metal anode with liquid electrolytes often comes with several disadvantages such as unwanted side reactions and uncontrolled dendritic growth, leading to short circuit and thermal runaway under extreme circumstances[6, 8, 9]. In this regard, solid-state batteries (SSBs) are a promising candidate to enable next-generation energy storage systems[10, 11]. Solid electrolytes (SEs), owing to their mechanical rigidity, can suppress the growth of lithium dendrites[12, 13]. Inorganic SEs also promise to improve the thermal stability window, thereby overcoming challenges such as leakage and flammability pertaining to liquid electrolytes[14-16]. Moreover, owing to their single-ion conducting nature, SEs avert the issue of concentration polarization which prevails in liquid electrolytes[17]. Despite such underlying advantages, development of SSBs is rife with several fundamental challenges concerning both the Li-metal anode and composite cathode[18-22].

Although mechanical rigidity of SEs promises to suppress lithium dendrite growth, recent experimental studies have observed internal short circuit due to metal penetration at several operating conditions[23-26]. Researchers have proposed several factors responsible for such failure, including structural heterogeneities of SE such as grain/grain boundaries and surface defects[27-29].

Distinct transport and mechanical properties of inorganic SEs in grains and grain boundaries lead to heterogeneous electrochemical-mechanical interactions promoting filament growth. In this regard, a recent study by Vishnugopi *et al.*[30] proposed that non-uniform electrodeposition at the anode-SE interface can lead to either cavities or protrusions at grain boundaries depending on their transport characteristics. Researchers have also observed metal penetration along grain boundaries in polycrystalline LLZO[24]. In addition, filament growth/propagation and internal short circuit strongly depends on microstructural attributes such as pore connectivity and density in SEs, whose dependency can be traced back to SE processing conditions[31]. Preferential plating due to pre-existing surface defects can result in crack propagation and thus, mechanical failure within SEs, as proposed by Porz *et al*[29]. Moreover, nucleation and filament penetration have also been observed near electrode edges owing to strong electric fields in their vicinity[32]. Non-zero electronic conduction in SEs like $Li_7La_3Zr_2O_{12}$ and Li_3PS_4 has been observed to be responsible for isolated lithium deposition within the bulk SE[33, 34]. Effect of molar volumes and stress fields on deposition stability during charging has been analyzed in detail in the recent past[35, 36]. Based on the molar volume mismatch and stress distribution, competing effects of mechanical overpotential and stress-driven ionic transport can result in either stable or unstable electrodeposition[37]. Sustained stability of the anode-SE interface over large number of cycles becomes critical for safe and efficient operation of SSBs. In this regard, extensive research has been conducted in recent years to study the evolution of anode-SE interface due to repeated deposition and dissolution during charging and discharging, respectively[38-41]. Interfacial contact area loss due to incomplete replenishment of Li during discharge operation leads to current focusing, which further instigates morphological instability during charging, resulting in filament growth and mechanical failure of SE[42-44]. Despite recent advancements in understanding various phenomena related to interfacial

instability, the effect of cathode architecture and the SE separator design on reaction heterogeneity at the anode-SE interface and its critical implications on interfacial instability still need to be addressed.

Cathode architecture plays a crucial role in dictating the electrochemical performance of SSBs[45]. Composition and spatial arrangement of the constituent phases (active material (AM), SE, carbon additives, binder and voids) dictate transport and kinetic signatures of the composite cathode[46-48]. To achieve high energy and power densities in SSBs, thicker cathodes with high AM loading along with minimal transport and kinetic resistances are required[49]. In this regard, several research efforts have been made to understand the influence of cathode design parameters such as composition, size, and morphologies of the constituent phases and electrode thickness[50-53]. Also, achieving thin SE separators in SSBs has been a topic of great interest as thick SE separators pose negative implications on ionic transport and energy density of SSBs[54]. In addition, cathode microstructural stochasticity has a significant effect on ionic transport through SE separator, especially during operational extremes[55]. Thus, investigating the influence of microstructural stochasticity of the composite cathode on ionic transport in the SE separator and its concomitant implications on anode stability and reaction kinetics at the anode-SE interface is hypothesized to be paramount.

In this work, we delineate the role of cathode architecture in reaction heterogeneity and its implications in anode stability. We present how various cathode microstructural attributes intricately govern reaction heterogeneity at the anode-separator interface. Effect of temperature on the anode-cathode crosstalk is also examined in detail by highlighting the role of temperature in attenuating heterogeneity propagation from the cathode to the anode. Influence of cathode loading and separator thickness on both the reaction heterogeneity and the energy density is investigated. Achieving higher energy density via increasing cathode loading or decreasing separator thickness

poses a major compromise on the anode stability due to highly heterogeneous reaction kinetics at the anode-separator interface. Thus lastly, we propose potential electrode design strategies to address this tradeoff between energy density and reaction heterogeneity in SSBs. This work provides mechanistic insights into cathode-anode crosstalk involving heterogeneity propagation through SE separator and improvement in energy densities of SSBs via electrode engineering.

2. Methodology:

Figure 1(a) shows a schematic illustration of SSB comprising of composite cathode, SE separator and Li-metal anode, where composite cathode consists of NMC622 AM, β-Li_3PS_4 SE, PVDF/C carbon-binder domain (CBD), and voids. During charging, electrochemical reactions occur at AM-SE interfaces in the composite cathode, where Li atoms are converted to Li^+ ions. These ions are then transported through the tortuous pathways of the SE phase in the composite cathode and then through the SE separator to reach the Li-metal anode where they are reduced back to Li atoms. Cathode-separator interface plays a critical role in ionic transport from composite cathode to Li-metal anode, as the intrinsic microstructural stochasticity of the cathode-separator interface defines the current heterogeneity which propagates through the SE separator and results in heterogeneous reaction distribution at the anode-separator interface. Thus, developing a modeling framework cognizant of the microstructural information at the cathode-separator interface to investigate the heterogeneity propagation from cathode to anode via ionic transport in the SE separator is necessary. As shown in Figure 1(a), the cathode-separator and anode-separator interfaces define the boundary conditions for ionic transport through the SE separator. Composite cathode microstructures are obtained using GeoDict reconstruction[56, 57], from which the microstructural information at the cathode-separator interface is extracted and used to define the boundary condition for ionic transport through the SE separator, as shown in Figure 1(b). For all composite

cathode microstructures reconstructed in this work, 20% of the total volume is assumed to be collectively occupied by the CBD phase and voids. The governing equation for ionic transport in the SE separator is given as follows:

$$\nabla.(k^{eff}\nabla\phi_{SE}) = 0 \tag{1}$$

Here, ϕ_{SE} is the electric potential in SE and k^{eff} is the effective ionic conductivity of SE in separator which can be obtained as follows:

$$k^{eff} = k\frac{\varepsilon_{SE}}{\tau_{SE}} \tag{2}$$

where, k is the intrinsic ionic conductivity of SE, ε_{SE} and τ_{SE} are the volume fraction and tortuosity of SE phase in separator, respectively. It is noted that the model takes long-range ionic transport into account as described by Eq. 1, while the atomistic scale stochastic redistribution of ions due to ion hopping is not explicitly considered assuming it has negligible effect on the electrode scale heterogeneities. Boundary condition at the cathode-separator interface is obtained using charge conservation as follows:

$$I_{app} = a_{total}i_{app} = a_{SE}i_{SE} + a_{AM}i_{AM} \tag{3}$$

where, I_{app} is the total current in Amperes (A), a_{total} is the total cross-sectional area of the cathode-separator interface, i_{app} is the applied current density, a_{SE} and a_{AM} are the cross-sectional areas occupied by the SE and AM phases, respectively at the cathode-separator interface, i_{SE} is the current density through SE phase at the cathode-separator interface and i_{AM} is the current density contributed by the electrochemical reactions occurring at the cathode-separator interface due to AM-SE contact (Figure 1(c)). Boundary condition at the anode-separator interface is given by Butler-Volmer kinetics as follows:

$$I_{app} = a_{total} i_{BV} = a_{total} i_0 \left(\exp\left(\frac{F\eta}{2RT}\right) - \exp\left(-\frac{F\eta}{2RT}\right)\right) \quad (4)$$

where, i_0 is the exchange current density, F is Faraday constant, R is universal gas constant and T is the temperature (K). Total ionic current at the cathode-separator interface has two components: (a) I_{AM}, arising from electrochemical reactions occurring specifically at the cathode-separator interface due to AM-SE contact, and (b) I_{SE}, ionic current carried by the SE phase at the cathode-separator interface, which originates from the electrochemical reactions occurring at the active interfacial sites in the bulk of the cathode. Figure 1(c) depicts the dynamic evolution of I_{AM}/I_{app} and I_{SE}/I_{app} for applied current of 5 mA/cm^2 and cathode composition of 60 vol. % AM and 20 vol. % SE. The results shown in Figure 1(c) are obtained using macro-homogeneous SSB model, which has been developed in our previous work[48]. From Figure 1(c), it is evident that almost all the ionic current flowing from cathode to separator is focused on the regions having SE phase at the cathode-separator interface. Fundamentally, the regions with SE phase at the cathode-separator interface carries the ionic current which originates from all the electrochemical reactions occurring in the bulk of the cathode (see Figure S2 of the Supporting Information). Whereas the regions with AM phase at the cathode-separator interface contribute only a small fraction of the ionic current which is derived from the electrochemical reactions between AM (at cathode-separator interface) and SE (of the separator). Moreover, towards the later stages of the charging process, when AM at the cathode-separator interface is completely delithiated, all the current will be contributed by the regions having SE phase at the cathode-separator interface (see Figure 1(c)). Thus, to account for the most extreme scenario, where the reaction heterogeneity is the highest during charging, ionic current is assumed to be carried entirely by the regions having SE phase at the cathode-

separator interface. This has been expounded in Section S4 of the Supporting Information. Thus, Eq. 3 is simplified as follows:

$$I_{app} = a_{total} i_{app} = a_{SE} i_{SE} \tag{5}$$

Variation of the ionic conductivity of SE with temperature follows Arrhenius equation and is incorporated in the model as follows:

$$\kappa = \kappa_0 \exp\left[\frac{E_{a,\kappa}}{R}\left(\frac{1}{T} - \frac{1}{T_{ref}}\right)\right] \tag{6}$$

Here, κ_0 is the intrinsic ionic conductivity of SE at reference temperature (T_{ref}) and $E_{a,\kappa}$ is the activation energy. Numerical values of κ_0 and $E_{a,\kappa}$ for β-Li_3PS_4 SE are extracted from a recent experimental report[58] and are given in Table S1 of the Supporting Information. Corresponding Arrhenius plot has been provided in Figure S1 of the Supporting Information.

Later in this work, we explain the tradeoff between reaction heterogeneity and energy density of SSBs, where theoretical volumetric energy density, E_v, of SSB is obtained as follows:

$$E_v = \frac{V_{cell} \times m_{AM} \times C_0}{\frac{m_{AM}}{\rho_{AM}} + \frac{m_{SE}}{\rho_{SE}} + \frac{m_{CBD}}{\rho_{CBD}} + \frac{m_a}{\rho_a} + V_{voids} + \frac{m_{Cu}}{\rho_{Cu}} + \frac{m_{Al}}{\rho_{Al}}} \tag{7}$$

Here, V_{cell} is the operating cell voltage, m_{AM} and ρ_{AM} are mass and density of AM, respectively, C_0 is the nominal capacity of AM, V_{voids} is the volume occupied by voids, m_{SE}, m_{CBD}, m_a, m_{Cu} and m_{Al} are the masses of SE, CBD, anode, copper current collector and aluminum current collector, respectively and ρ_{SE}, ρ_{CBD}, ρ_a, ρ_{Cu} and ρ_{Al} are the corresponding material densities. All the properties and parameters used in the modeling framework are listed in Table S1 of the Supporting Information.

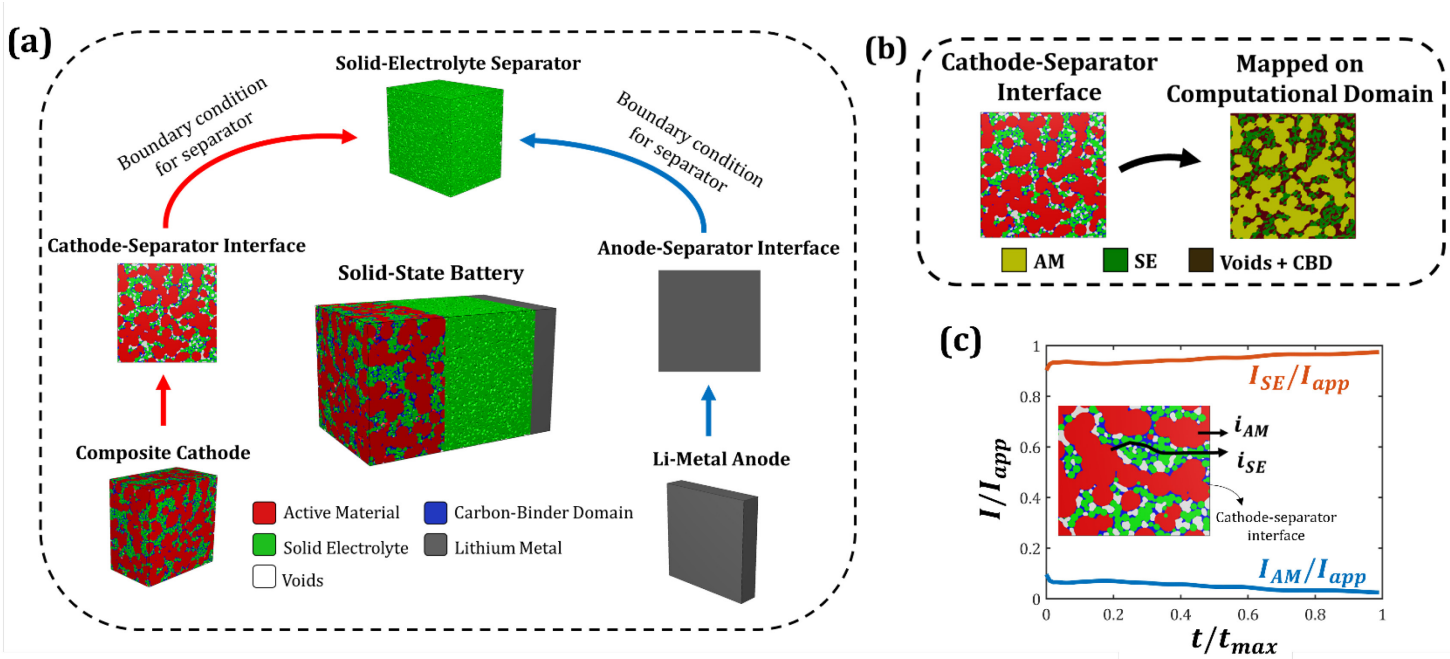

Figure 1. (a) Schematic illustration of SSB consisting of composite cathode, SE separator, and Li-metal anode, along with schematic representation of the boundary conditions for ionic transport in SE separator. (b) Cathode-separator interface obtained is fed as boundary condition to solve for ionic transport in SE separator by tracking all the constituent phases of composite cathode, namely, AM, SE, CBD, and voids. (c) Fraction of the total current contributed by the regions with AM phase and the regions with SE phase at the cathode-separator interface as a function of time for the applied current of 5 mA/cm^2 and cathode composition of 60 vol. % AM, 20 vol. % SE and 20 vol. % CBD and voids.

3. Results and discussions:

As shown in Figure 1(c), the SE phase at the cathode-separator interface carries majority of the total current from cathode to separator during the charging process. This leads to current-focusing at the locations having SE phase, resulting in heterogeneous distribution of current at the cathode-separator interface. Such spatial heterogeneity in ionic current can propagate through the separator and cause spatially uneven electrochemical reactions at the anode-separator interface of an SSB. The extent of this reaction heterogeneity is highly dependent on the cathode composition, as depicted in Figure 2. Material map of a composite cathode at the cathode-separator interface has been shown for cathode compositions of 40 vol. % AM and 40 vol. % SE (Figure 2(b)), 50 vol. %

AM and 30 vol. % SE (Figure 2(c)), and 60 vol. % AM and 20 vol. % SE (Figure 2(d)), followed by the corresponding current distribution at the cathode-separator and the anode-separator interfaces for applied current density of 5 mA/cm^2 and separator thickness of 40μm. As the AM loading is increased, current-focusing on the cathode-separator interface intensifies owing to smaller SE fraction, as evident from the current heterogeneity maps shown in Figure 2(b-d). This current heterogeneity arising from the inherent stochasticity of the composite cathode translates through the separator and shows up on the anode-separator interface as represented via reaction heterogeneity maps in Figure 2(b-d). For the AM loading of 40% (Figure 2(b)), the maximum (i_{max}) and minimum (i_{min}) local reaction currents at the anode-separator interface are 5.6 mA/cm^2 and 4.7 mA/cm^2 respectively, whereas for the AM loading of 50% (Figure 2(c)) and 60% (Figure 2(d)), i_{max} and i_{min} are 5.7 mA/cm^2, 4.6 mA/cm^2 and 6.1 mA/cm^2, 4.5 mA/cm^2 respectively. The difference between the maximum and minimum local reaction current densities, $i_{max} - i_{min}$, can be taken as a measure of reaction heterogeneity prevailing at the anode-separator interface. Figure 2(a) represents $i_{max} - i_{min}$ as a function of AM loading where the reaction heterogeneities for five distinct cathode microstructures have been plotted for each cathode composition and the average trend in the heterogeneity is depicted using the black line. It is noted that current heterogeneity for the same cathode composition can be different for different cathode microstructures owing to dissimilar microstructural stochasticity. From Figure 2(a), it is clear that reaction heterogeneity at the anode-separator interface intensifies at higher cathode AM loading. Hence, employing high energy density cathodes in SSB can escalate the uneven electrochemical interactions at the Li-metal anode, leading to non-uniform electrodeposition during charging, resulting in deleterious implications on the stability of the anode-separator interface. This heterogeneity cross-talk between the high energy density cathode and Li-metal anode occurring

due to inherent stochasticity of the cathode-separator interface is further investigated in the subsequent sections.

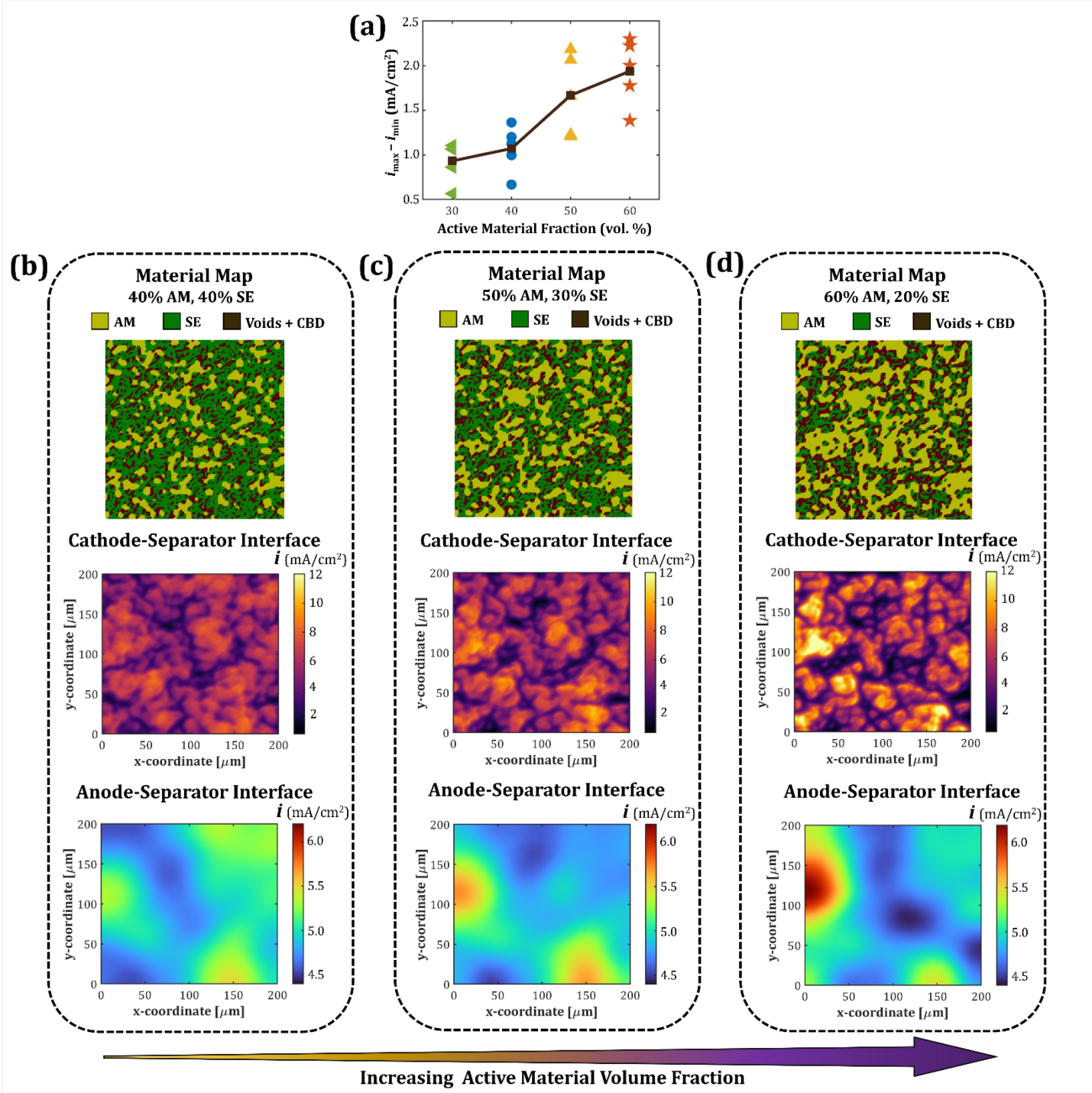

Figure 2. (a) Reaction heterogeneity at the anode-separator interface quantified via the difference between the maximum and the minimum local reaction current ($i_{max} - i_{min}$) as a function of cathode AM volume fraction for an applied current density of 5 mA/cm^2. Reaction heterogeneity has been plotted for five distinct cathode microstructures at each cathode composition, while the

black line denotes the average trend with increase in AM loading. Material maps showing the spatial distribution of constituent phases of the composite cathode (AM, SE, CBD + voids) at the cathode-separator interface and current distribution at the cathode-separator and anode-separator interfaces for cathode compositions of (b) 40 vol. % AM, 40 vol. % SE, (c) 50 vol. % AM, 30 vol. % SE, and (d) 60 vol. % AM, 20 vol. % SE for separator thickness of 40μm.

In Figure 3, the effect of AM and SE particle sizes on reaction heterogeneity at the anode-separator interface has been investigated for applied current density of 5 mA/cm^2, separator thickness of 40μm, and cathode composition of 60 vol. % AM and 20 vol. % SE. With increase in AM particle size, reaction heterogeneity at the anode-separator interface intensifies, as seen from the average trend in Figure 3(a). For AM diameter of 8μm, average heterogeneity ($i_{max} - i_{min}$) is 1.6 mA/cm^2, whereas for AM diameter of 21μm, average $i_{max} - i_{min}$ is as high as 3.4 mA/cm^2, suggesting that cathode AM size significantly influences the reaction heterogeneity at the anode-separator interface. Material map of the cathode-separator interface and current distribution at the cathode-separator and anode-separator interfaces are shown for AM diameters of 8μm and 21μm in Figure 3(c). As seen from the material map, due to the larger size of AM particles, the AM phase occupies bigger chunks of space at the cathode-separator interface. Consequently, the SE phase is more localized, resulting in severe current focusing on the regions containing SE phase at the cathode-separator interface, leading to significant reaction heterogeneity on the anode side (Figure 3(c)). On the other hand, spatial distribution of the constituent phases of cathode with smaller AM particles is relatively more uniform, resulting in moderate current heterogeneities at the cathode-separator and anode-separator interfaces (Figure 3(c)). Figure 3(b) shows the effect of SE particle size on reaction heterogeneity at the anode, where SE particle diameter is varied from 2μm to 8μm. It is observed that current heterogeneity increases with increase in SE diameter, but the effect is not as severe as seen for increasing AM diameter (Figure 3(a)). This is attributed to the smaller sizes of SE particles (2μm - 8μm) as compared to AM particles (8μm - 21μm). While smaller SE

particles can be more evenly distributed, larger SE particles occupy bigger chunks of the space on the cathode-separator interface simultaneously leading to the localized regions without SE phase (see Figure S5 of the Supporting Information). Thus, similar to the larger AM size case, localization of the SE phase at the cathode-separator interface for larger SE particles leads to current-focusing, which translates to the anode side as shown in Figure 3(d). Overall, utilizing smaller AM and SE particles can ameliorate the problem of current heterogeneity propagating from cathode to anode during the charging process. Also, the cathode microstructure with smaller/larger SE particles will have more/less grain boundaries. Thus, it is noted that, owing to the distinct transport properties of the grain and grain boundaries, grain boundaries can influence the current distribution at the cathode-separator interface and subsequently affect the reaction heterogeneity on the anode side.

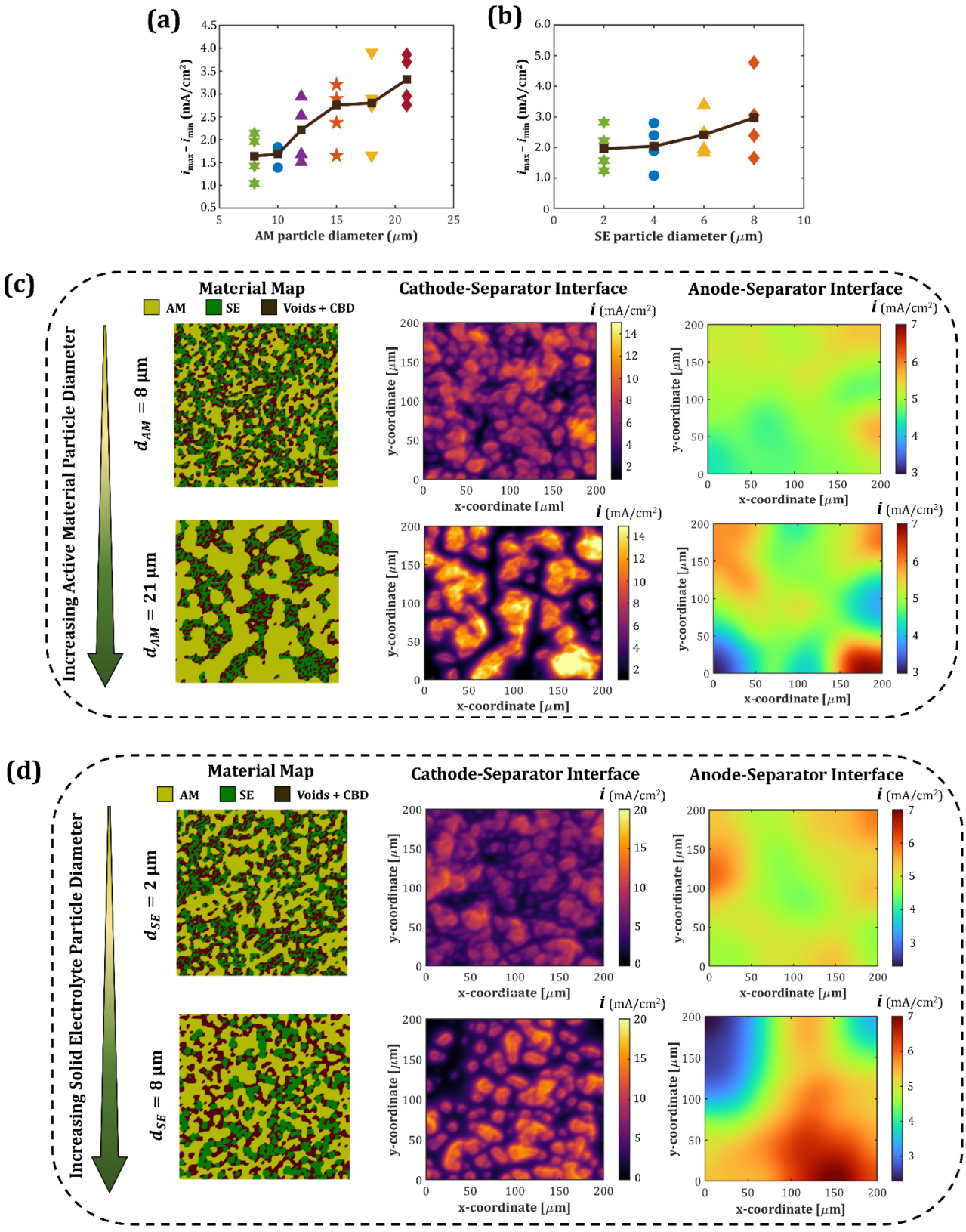
(a)
$i_{max} - i_{min}$ (mA/cm²)
AM particle diameter (μm)
(b)
$i_{max} - i_{min}$ (mA/cm²)
SE particle diameter (μm)
(c)
Material Map
AM
SE
Voids + CBD
Increasing Active Material Particle Diameter
d_{AM} = 8 µm
d_{AM} = 21 µm
Cathode-Separator Interface
Anode-Separator Interface
i (mA/cm²)
y-coordinate [μm]
x-coordinate [μm]
(d)
Material Map
AM
SE
Voids + CBD
Increasing Solid Electrolyte Particle Diameter
d_{SE} = 2 µm
d_{SE} = 8 µm
Cathode-Separator Interface
Anode-Separator Interface
i (mA/cm²)
y-coordinate [μm]
x-coordinate [μm]

Figure 3. Reaction heterogeneity at the anode-separator interface quantified via $i_{max} - i_{min}$ as a function of (a) AM and (b) SE particle diameter for applied current density of 5 mA/cm^2, cathode composition of 60 vol. % AM, 20 vol. % SE and separator thickness of 40μm. Material maps at the cathode-separator interface, current distribution at the cathode-separator and anode-separator interfaces for (c) AM particle diameter of 8μm and 21μm and (d) SE particle diameter of 2μm and 8μm, respectively.

Ionic conductivity of SE strongly depends on temperature. Thus, temperature can significantly affect ionic transport in the SE separator, having concomitant influence on reaction heterogeneity at the anode-separator interface. Variation of ionic conductivity of β-Li_3PS_4 SE with temperature follows the Arrhenius equation and has been experimentally probed in previous studies[58-60], where it is found to vary from 0.001 S/m at $-20\,^0$C to 0.04 S/m at $60\,^0$C, which is a 40-fold increase. In Figure 4, the effect of cell temperature on reaction heterogeneity at the anode-separator interface has been presented. Figure 4(a) represents reaction heterogeneity at the anode-separator interface for cell temperatures of $0\,^0$C and $60\,^0$C, respectively for applied current density of 5 mA/cm^2, cathode composition 60 vol. % AM, 20 vol. % SE and separator thickness 40μm. At lower cell temperatures, lower ionic conductivity of SE hinders ionic conduction in in-plane directions (x and y directions), causing inherent current heterogeneity at the cathode-separator interface to propagate through the separator and prevail at the anode-separator interface, as evident from the reaction heterogeneity maps shown in Figure 4(a). For cell temperature of $-20\,^0$C, reaction heterogeneity ($i_{max} - i_{min}$) at the anode-separator interface is 2.6 mA/cm^2, while at $60\,^0$C it decreases to 1.7 mA/cm^2 as shown in Figure 4(b), owing to efficient ionic conduction in the SE separator. Also, it is noted that the impact of temperature on the reaction heterogeneity is quite significant at high temperature regime ($40\,^0$C to $60\,^0$C) as compared to low temperature regime ($-20\,^0$C to $0\,^0$C). For instance, reaction heterogeneity decreases by 0.1 mA/cm^2 as temperature is increased from $-20\,^0$C to $0\,^0$C, whereas it decreases by almost 0.4 mA/cm^2 as temperature is increased from $40\,^0$C to $60\,^0$C. This trend is majorly related to the variation of ionic conductivity

of SE with temperature. Due to the high thermal stability of SEs, thermally assisted improvement in ionic transport can serve as a potential strategy to homogenize electrochemical reactions at the anode-separator interface while employing high energy density cathodes.

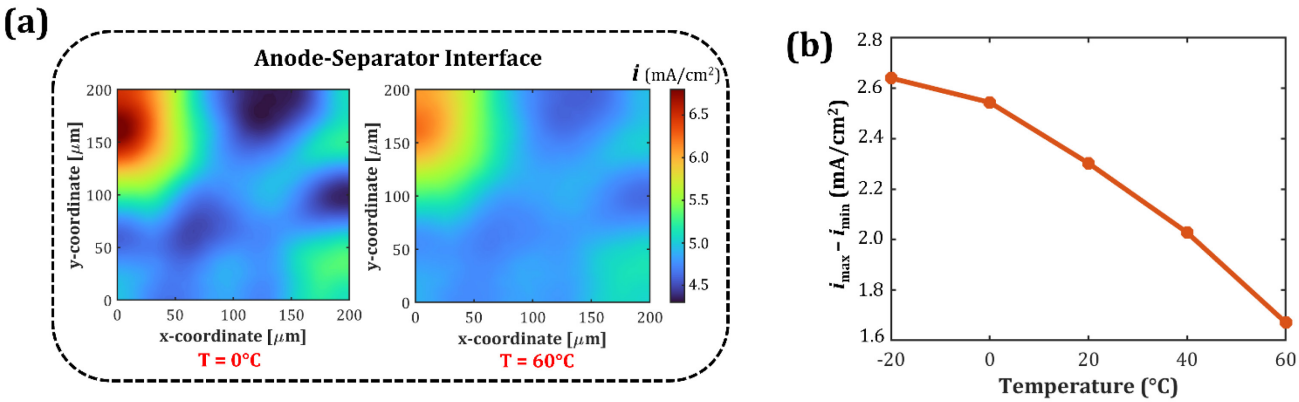

Figure 4. (a) Reaction distribution at the anode-separator interface for cell temperatures of $0\,^{0}$C and $60\,^{0}$C, respectively for applied current density of 5 mA/cm^2, cathode composition 60 vol. % AM, 20 vol. % SE and separator thickness 40μm. (b) Reaction heterogeneity ($i_{max} - i_{min}$) at the anode-separator interface as a function of cell temperature.

With regards to the heterogeneity cross-talk between the cathode-separator and anode-separator interfaces, separator thickness plays a critical role. In this section, the effect of separator thickness on heterogeneity propagation from cathode to anode has been extensively probed. Figure 5(a) depicts the reaction distribution at the anode-separator interface for separator thicknesses of 25μm and 75μm, respectively for applied current density of 5 mA/cm^2 and cathode composition of 60 vol. % AM, 20 vol. % SE. Reaction heterogeneity ($i_{max} - i_{min}$) for separator thickness 25μm is almost 4 mA/cm^2, while it drops down to 1 mA/cm^2 for separator thickness 75μm. Figure 5(a) corroborates the fact that increasing separator thickness can mitigate reaction heterogeneity at the anode-separator interface arising from inherent stochasticity in the cathode microstructure. To investigate further, Figures 5(b-d) represent the variation of reaction heterogeneity at the anode-separator interface as a function of separator thickness for varying cathode composition, AM

diameter and SE diameter respectively. As discussed in the earlier section, increasing AM loading as well as AM and SE diameters leads to severe current-focusing on the regions with SE phase at the cathode-separator interface, resulting in higher current heterogeneity, as also seen in Figures 5(b-d). As the separator thickness is increased, there is initially a steep drop in reaction heterogeneity, which slows down at higher thicknesses as shown in Figure 5(b-d). From Figure 5(b), it is also evident that enhancing energy density via increasing AM loading and decreasing separator thickness can have deleterious impact on anode stability due to severe heterogeneity in reaction kinetics at the anode-separator interface. To quantitatively mark the separator thickness at which the electrochemical reactions at the anode-separator interface become homogeneous, the critical separator thickness, L_c, is defined such that: at $L_{sep} = L_c, \frac{i_{max} - i_{min}}{i_{app}} = 0.05$. In other words, at critical separator thickness, the reaction heterogeneity at the anode-separator interface ($i_{max} - i_{min}$) is 5% of the applied current density. Black arrows in Figure 5(b-d) represent L_c for different cathode compositions and AM and SE sizes. With increase in AM loading, critical separator thickness significantly increases. For instance, L_c for cathode composition of 30 vol. % AM, 50 vol. % SE is 75μm, whereas it is 150μm for cathode composition of 60 vol. % AM, 20 vol. % SE. Similarly, critical separator thickness increases with increase in AM and SE sizes as shown in Figure 5(c-d). Figure 5(e) represents the variation of non-dimensional reaction heterogeneity, $\frac{i_{max} - i_{min}}{i_{app}}$ with separator thickness for different applied current densities. It is interesting to note that the increase in critical separator thickness with increasing applied current density is negligible. For e.g., L_c is 143μm for applied current density 1 mA/cm^2 and 148μm for 10 mA/cm^2. Figures 5(b-e) suggest that the critical separator thickness of an SSB depends on intrinsic parameters such as cathode composition, AM and SE particle morphologies and SE ionic conductivity (Figure 4) and is independent of extrinsic parameters like applied current density. Thus, to minimize the

critical separator thickness, a deeper dive into the design aspects of composite cathodes is crucial. Also, from the observed values of the critical separator thicknesses, it can be clearly seen that stochastic cathode architectures can require high separator thicknesses ($\sim 150\mu$m) to achieve homogeneous electrochemical reactions at the anode-separator interface. This presents a clear trade-off between energy density of SSB versus reaction homogeneity on the anode side. Moreover, high values separator thickness also leads to poor ionic percolation within SE separator, thus increasing the ion transport resistance during the cell operation. This trade-off between energy density and ion transport resistance versus reaction homogeneity can be addressed to a significant extent using architected cathodes, which is discussed in detail in the next section.

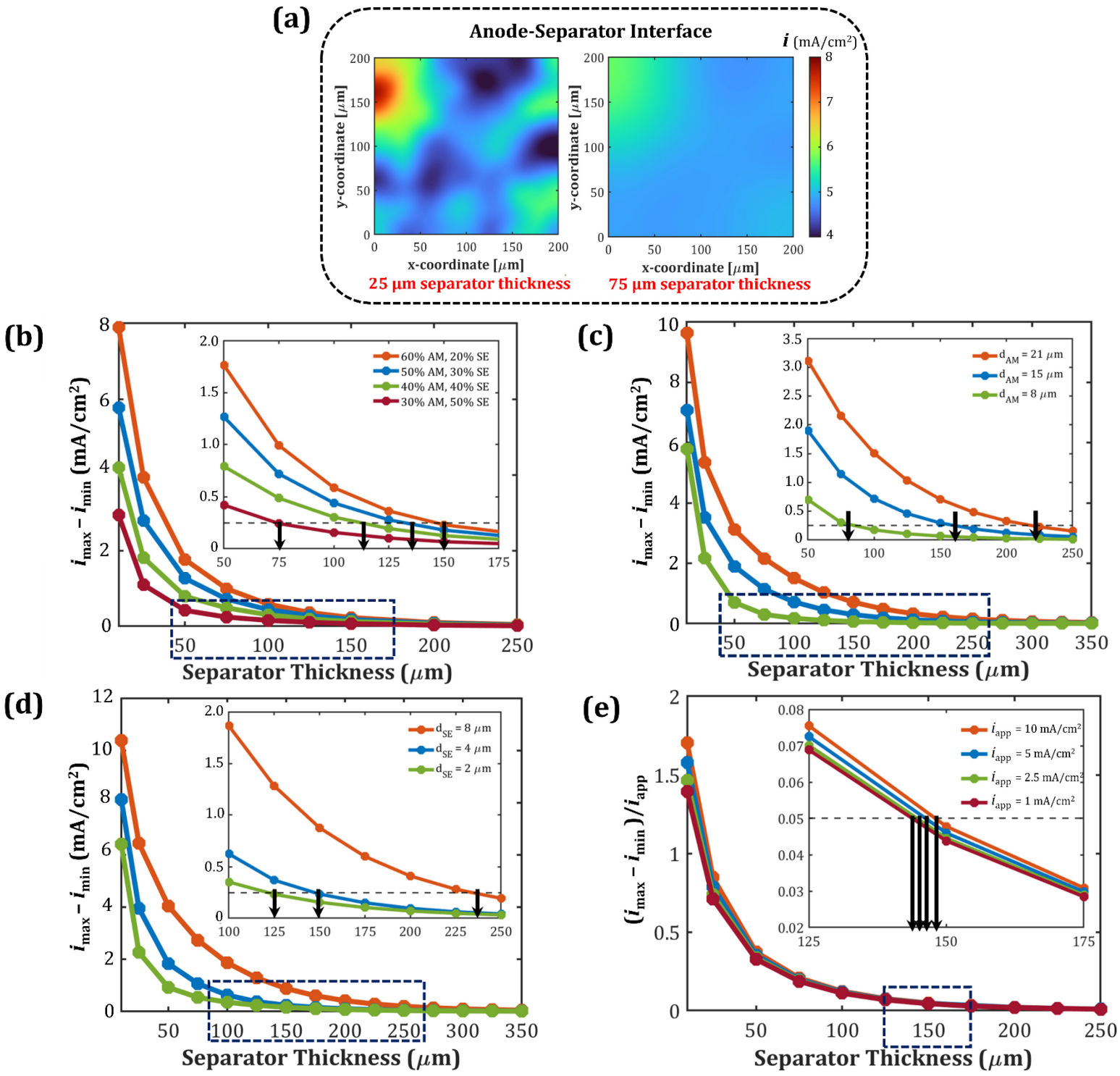

Figure 5. (a) Reaction distribution at the anode-separator interface for separator thicknesses of 25μm and 75μm, respectively for applied current density of 5 mA/cm^2 and cathode composition of 60 vol. % AM, 20 vol. % SE. Reaction heterogeneity ($i_{max} - i_{min}$) at the anode-separator interface as a function of separator thickness for different (b) cathode compositions, (c) AM particle diameters, and (d) SE particle diameters. (e) Non-dimensional reaction heterogeneity,

$(i_{max} - i_{min})/i_{app}$, at the anode-separator interface as a function of separator thickness for varying applied current densities at cathode composition of 60 vol. % AM, 20 vol. % SE.

In Figure 6, the potential of architected cathodes to achieve homogenized electrochemical reactions at the anode-separator interface is explored. Architected cathode microstructures in this work are obtained by repeating the microstructural arrangement of constituent phases at every 20μm interval in both x and y directions (Figure 6(b)). Figure 6(a) and Figure 6(b) represent the material map at the cathode-separator interface and current distribution at the cathode-separator and anode-separator interfaces for stochastic and architected cathode designs, respectively. Reaction distribution at the anode-separator interface follows the stochastic nature of cathode in Figure 6(a), whereas it is almost homogeneous for the architected cathode (Figure 6(b)) for separator as thin as 25μm. To further this analysis, Figure 6(c) compares the reaction heterogeneity $(i_{max} - i_{min})$ at the anode-separator interface for stochastic and architected cathodes for varying separator thickness. Especially at thin separator regime, remarkable reduction in reaction heterogeneity is observed for the architected cathode. For instance, with a separator thickness of 25μm, reaction heterogeneity $(i_{max} - i_{min})$ is 4 mA/cm^2 for the stochastic cathode, whereas it drops to 0.8 mA/cm^2 for the architected cathode. Moreover, critical separator thickness, L_c, for stochastic and architected cathodes is 150μm and 75μm, respectively (as marked with the black arrows in Figure 6(c)) which suggests 43% increase in the volumetric energy density of SSB while utilizing architected cathode (see Figure 7). Thus, architected cathode designs show promise to minimize the separator thickness while employing high energy density cathode designs, thereby significantly boosting the energy density of SSBs, yet achieving homogeneous electrochemical reactions at the anode-separator interface. Also, utilizing architected cathodes promise to mitigate the ion transport limitations in both composite cathode (via reducing ionic tortuosity) and SE separator (via minimizing the separator thickness).

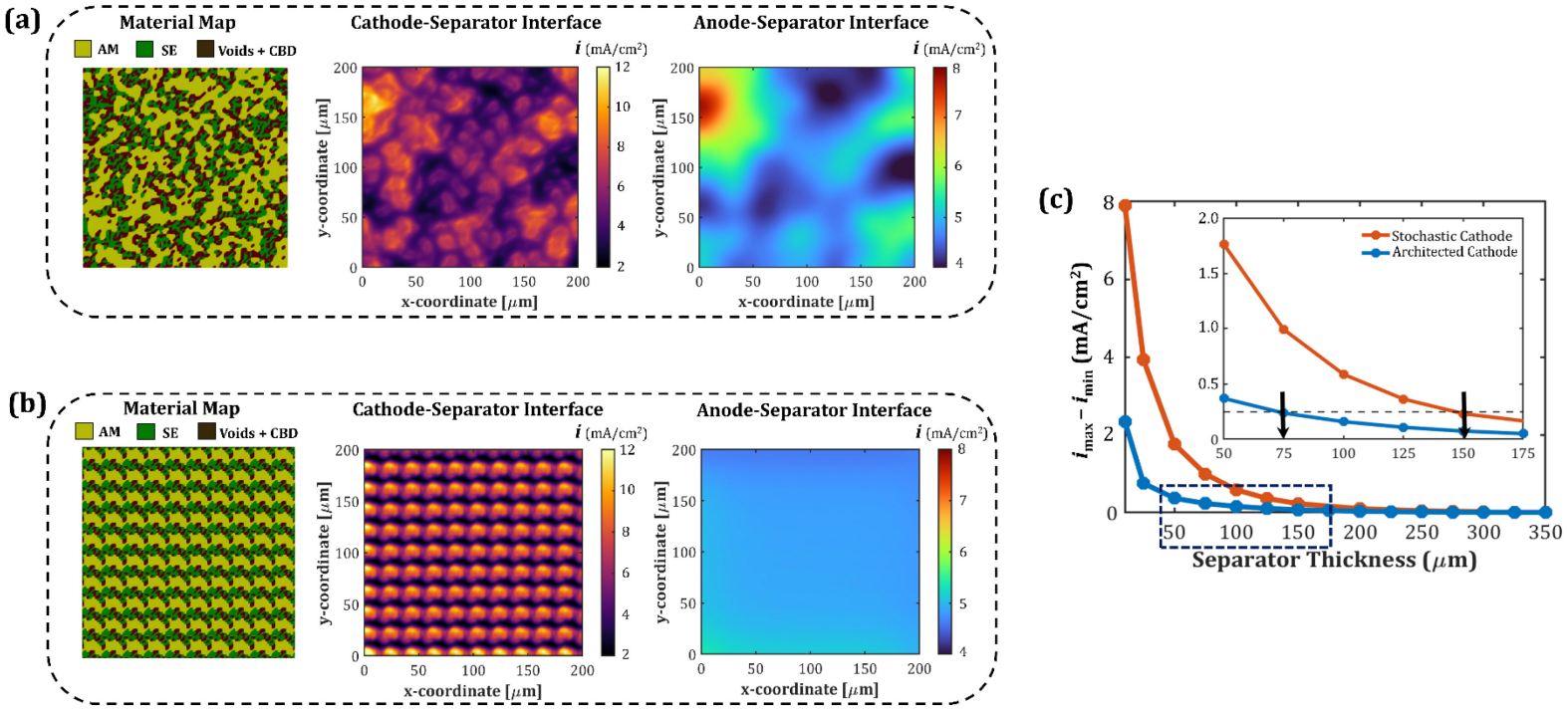

Figure 6. Material map of cathode-separator interface, current distribution at cathode-separator and anode-separator interfaces for (a) stochastic cathode and (b) architected cathode with composition 60 vol. % AM, 20 vol. % SE for applied current density 5 mA/cm^2 and separator thickness 25μm. (c) Reaction heterogeneity ($i_{max} - i_{min}$) at the anode-separator interface as a function of separator thickness for stochastic and architected cathodes taken in (a) and (b), respectively.

In Figures 7(a-c), theoretical energy density, E_v, of SSB and reaction homogeneity, θ, at the anode-separator interface for stochastic and architected cathode designs is depicted as a function of AM loading and separator thickness. Here, reaction homogeneity, θ, is defined as follows:

$$\theta = \frac{i_{app}}{(i_{max} - i_{min}) + i_{app}} \tag{8}$$

From Eq. 8, it is clear that θ is always less than or equal to 1, where $\theta = 1$ corresponds to perfectly homogeneous electrochemical interactions at the anode-separator interface. Increasing AM loading and decreasing separator thickness increases the theoretical energy density of SSBs (Figure 7(a)), but at the same time negatively affects the reaction homogeneity at the anode-

separator interface as shown in Figure 7(b). In this regard, architected cathode designs can help address the trade-off between energy density and reaction homogeneity by minimizing the separator thickness required for achieving homogeneous electrochemical reactions at the anode-separator interface (Figure 7(c)). At thin separator regime, there is a remarkable improvement in reaction homogeneity (θ) for the architected cathode. For instance, reaction homogeneity for separator thickness of 20μm and cathode composition with AM loading of 60 vol. % is 0.9 for architected cathode, which is 80% improvement as compared to the stochastic cathode case ($\theta = 0.5$). Also, with increasing AM loading for a particular separator thickness (less than 100μm), reaction homogeneity decreases rapidly for the stochastic cathode, whereas it is almost unaffected for the architected cathode. Moreover, reaction homogeneity of 0.95 is marked in Figure 7(b) and 7(c), above which the electrochemical reactions at the anode-separator interface can be considered almost homogeneous. A significant reduction in the separator thickness can be achieved using the architected cathode design, especially at high AM loadings. For example, at AM loading of 60 vol. %, $\theta = 0.95$ is achieved at separator thickness of 145μm for the stochastic cathode and 70μm for the architected cathode design. Trends observed in Figure 7 show potential of architected cathode to achieve high AM loading composite cathodes without compromising the reaction homogeneity at the anode-separator interface. Thus, architected cathode designs can potentially enable achieving high energy density SSBs by simultaneously allowing the use of energy-dense cathodes and thin separators, while maintaining interfacial stability at the anode-separator interface. In addition to the architected cathodes discussed above, dense cathode architectures proposed in the recent report[61], where the electrochemical reactions occur only at the cathode-separator interface (and not in the bulk of the cathode) can also potentially help in homogenizing the electrodeposition at the anode side. With the absence of SE phase in such cathode architectures, localization of the

ionic current at the cathode-separator interface can be prevented, thus enabling uniform ionic current through the SE separator. Enhancing self-diffusion kinetics, creep, and plastic flow of the lithium metal via modulating extrinsic parameters such as temperature and pressure can also be a potential strategy to achieve uniform interface during electrodeposition[30]. Moreover, incorporating an interlayer which exhibits enhanced transport characteristics[62] and has ability to lower the nucleation overpotential for lithium[63] can also help in achieving homogeneous electrodeposition.

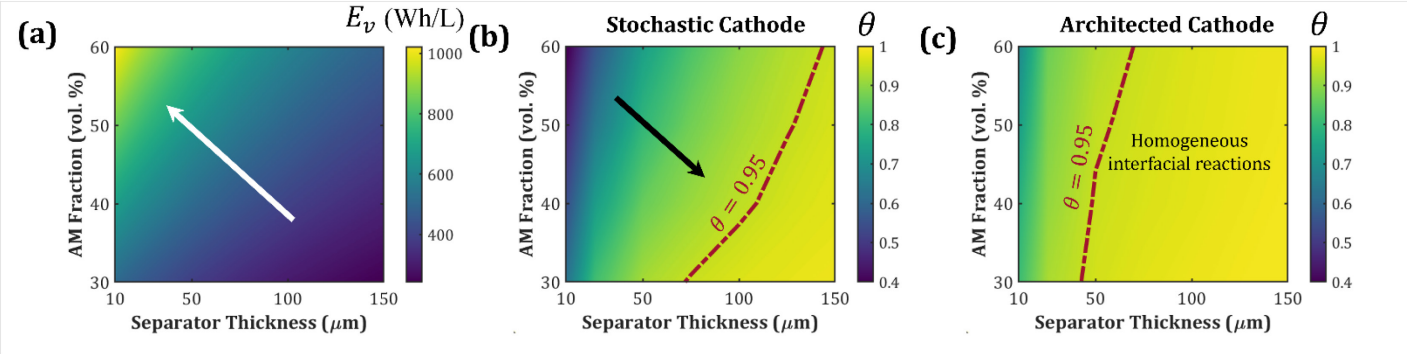

Figure 7. (a) Theoretical energy density of an SSB as a function of AM loading and separator thickness. Reaction homogeneity at the anode-separator interface for (b) stochastic and (c) architected cathode designs as a function of AM loading and separator thickness. Architected cathode design shows promise to address the trade-off between energy density and reaction homogeneity at anode-separator interface within SSBs with Li-metal anodes.

4. Conclusion:

Overall, this work provides key insights into the effect of cathode architecture and separator design on the reaction heterogeneity at the anode-separator interface. Achieving higher AM loading in composite cathodes come at a disadvantage of higher reaction heterogeneity at the anode-separator interface, contributing towards interfacial instability. Similarly, increasing AM and SE particle sizes in composite cathode can result in severe current focusing at the cathode-separator interface causing highly heterogeneous kinetic interactions on the anode side. In this regard, temperature can play a vital role in mitigating deleterious effects of inherent cathode stochasticity on the reaction kinetics at anode-separator interface, thus assisting towards utilization of higher AM

loading solid-state cathodes. Also, separator thickness has critical implications on the cathode-anode heterogeneity crosstalk. Decreasing separator thickness and/or increasing cathode loading for enhancing the energy density of SSBs significantly increases the reaction heterogeneity at anode-separator interface, leading to interfacial instability. Minimum separator thickness required to achieve homogeneous electrochemical reactions is found to be majorly dependent on the cathode architecture. Thus, to address aformentioned energy density-heterogeneity tradeoff, architected cathode designs can serve as potential strategies to increase energy density of SSBs by employing high AM loading composite cathodes and minimizing the separator thickness while preserving reaction homogeneity at anode-separator interface.

Acknowledgement:

Financial support in part from the National Science Foundation (award no.: 2041499) and the Alfred P. Sloan Foundation through a Scialog – Advanced Energy Storage award is gratefully acknowledged.

Conflict of Interest

There are no conflicts to declare.

Supporting Information

Table S1, list of properties and parameters used in the modeling framework; section S1, temperature dependent ionic conductivity of β-Li_3PS_4 solid electrolyte (SE); Figure S1, Arrhenius

plot for ionic conductivity of β-Li_3PS_4 SE; section S2, quantifying current distribution at the cathode-separator interface; Figure S2, schematic of a solid-state cathode depicting current distribution at the cathode-separator interface; section S3, reaction heterogeneity analysis for high active material loading cathode; Figure S3, analysis of reaction heterogeneity for high AM loading cathodes (80 vol. % AM); section S4, dynamic evolution of the heterogeneities at the electrode-separator interfaces; Figure S4, time evolution of the heterogeneities at the cathode-separator and anode-separator interfaces; Figure S5, spatial variability of the SE phase for small and large SE particles.

References:

1. Choi, J. W.; Aurbach, D., Promise and Reality of Post-Lithium-Ion Batteries with High Energy Densities. *Nature Reviews Materials* **2016,** *1* (4), 1-16.
2. Nitta, N.; Wu, F.; Lee, J. T.; Yushin, G., Li-Ion Battery Materials: Present and Future. *Materials today* **2015,** *18* (5), 252-264.
3. Goodenough, J. B.; Kim, Y., Challenges for Rechargeable Li Batteries. *Chemistry of materials* **2010,** *22* (3), 587-603.
4. Lin, D.; Liu, Y.; Cui, Y., Reviving the Lithium Metal Anode for High-Energy Batteries. *Nature nanotechnology* **2017,** *12* (3), 194-206.
5. Guo, Y.; Li, H.; Zhai, T., Reviving Lithium-Metal Anodes for Next-Generation High-Energy Batteries. *Advanced Materials* **2017,** *29* (29), 1700007.
6. Cheng, X.-B.; Zhang, R.; Zhao, C.-Z.; Zhang, Q., Toward Safe Lithium Metal Anode in Rechargeable Batteries: A Review. *Chemical reviews* **2017,** *117* (15), 10403-10473.
7. Xu, W.; Wang, J.; Ding, F.; Chen, X.; Nasybulin, E.; Zhang, Y.; Zhang, J.-G., Lithium Metal Anodes for Rechargeable Batteries. *Energy & Environmental Science* **2014,** *7* (2), 513-537.
8. Zheng, J.; Kim, M. S.; Tu, Z.; Choudhury, S.; Tang, T.; Archer, L. A., Regulating Electrodeposition Morphology of Lithium: Towards Commercially Relevant Secondary Li Metal Batteries. *Chemical Society Reviews* **2020,** *49* (9), 2701-2750.
9. Liu, B.; Zhang, J.-G.; Xu, W., Advancing Lithium Metal Batteries. *Joule* **2018,** *2* (5), 833-845.
10. Janek, J.; Zeier, W. G., A Solid Future for Battery Development. *Nature Energy* **2016,** *1* (9), 1-4.
11. Ulvestad, A., A Brief Review of Current Lithium Ion Battery Technology and Potential Solid State Battery Technologies. *arXiv preprint arXiv:1803.04317* **2018** (https://doi.org/10.48550/arXiv.1803.04317) (https://arxiv.org/abs/1803.04317, submitted March 12, 2018).
12. Hatzell, K. B.; Chen, X. C.; Cobb, C. L.; Dasgupta, N. P.; Dixit, M. B.; Marbella, L. E.; McDowell, M. T.; Mukherjee, P. P.; Verma, A.; Viswanathan, V., Challenges in Lithium Metal Anodes for Solid-State Batteries. *ACS Energy Letters* **2020,** *5* (3), 922-934.
13. Krauskopf, T.; Richter, F. H.; Zeier, W. G.; Janek, J. r., Physicochemical Concepts of the Lithium Metal Anode in Solid-State Batteries. *Chemical Reviews* **2020,** *120* (15), 7745-7794.

14. Liu, J.; Bao, Z.; Cui, Y.; Dufek, E. J.; Goodenough, J. B.; Khalifah, P.; Li, Q.; Liaw, B. Y.; Liu, P.; Manthiram, A., Pathways for Practical High-Energy Long-Cycling Lithium Metal Batteries. *Nature Energy* **2019,** *4* (3), 180-186.
15. Randau, S.; Weber, D. A.; Kötz, O.; Koerver, R.; Braun, P.; Weber, A.; Ivers-Tiffée, E.; Adermann, T.; Kulisch, J.; Zeier, W. G., Benchmarking the Performance of All-Solid-State Lithium Batteries. *Nature Energy* **2020,** *5* (3), 259-270.
16. Lee, Y.-G.; Fujiki, S.; Jung, C.; Suzuki, N.; Yashiro, N.; Omoda, R.; Ko, D.-S.; Shiratsuchi, T.; Sugimoto, T.; Ryu, S., High-Energy Long-Cycling All-Solid-State Lithium Metal Batteries Enabled by Silver–Carbon Composite Anodes. *Nature Energy* **2020,** *5* (4), 299-308.
17. Vishnugopi, B. S.; Kazyak, E.; Lewis, J. A.; Nanda, J.; McDowell, M. T.; Dasgupta, N. P.; Mukherjee, P. P., Challenges and Opportunities for Fast Charging of Solid-State Lithium Metal Batteries. *ACS Energy Letters* **2021,** *6* (10), 3734-3749.
18. Zhang, F.; Huang, Q.-A.; Tang, Z.; Li, A.; Shao, Q.; Zhang, L.; Li, X.; Zhang, J., A Review of Mechanics-Related Material Damages in All-Solid-State Batteries: Mechanisms, Performance Impacts and Mitigation Strategies. *Nano Energy* **2020,** *70*, 104545.
19. Kim, K. J.; Balaish, M.; Wadaguchi, M.; Kong, L.; Rupp, J. L., Solid-State Li–Metal Batteries: Challenges and Horizons of Oxide and Sulfide Solid Electrolytes and Their Interfaces. *Advanced Energy Materials* **2021,** *11* (1), 2002689.
20. Gao, Z.; Sun, H.; Fu, L.; Ye, F.; Zhang, Y.; Luo, W.; Huang, Y., Promises, Challenges, and Recent Progress of Inorganic Solid-State Electrolytes for All-Solid-State Lithium Batteries. *Advanced materials* **2018,** *30* (17), 1705702.
21. Xia, S.; Wu, X.; Zhang, Z.; Cui, Y.; Liu, W., Practical Challenges and Future Perspectives of All-Solid-State Lithium-Metal Batteries. *Chem* **2019,** *5* (4), 753-785.
22. Barai, P.; Rojas, T.; Narayanan, B.; Ngo, A. T.; Curtiss, L. A.; Srinivasan, V., Investigation of Delamination-Induced Performance Decay at the Cathode/Llzo Interface. *Chemistry of Materials* **2021,** *33* (14), 5527-5541.
23. Ren, Y.; Shen, Y.; Lin, Y.; Nan, C.-W., Direct Observation of Lithium Dendrites inside Garnet-Type Lithium-Ion Solid Electrolyte. *Electrochemistry Communications* **2015,** *57*, 27-30.
24. Cheng, E. J.; Sharafi, A.; Sakamoto, J., Intergranular Li Metal Propagation through Polycrystalline Li6. 25al0. 25la3zr2o12 Ceramic Electrolyte. *Electrochimica Acta* **2017,** *223*, 85-91.
25. Sharafi, A.; Meyer, H. M.; Nanda, J.; Wolfenstine, J.; Sakamoto, J., Characterizing the Li–Li7la3zr2o12 Interface Stability and Kinetics as a Function of Temperature and Current Density. *Journal of Power Sources* **2016,** *302*, 135-139.
26. Basappa, R. H.; Ito, T.; Yamada, H., Contact between Garnet-Type Solid Electrolyte and Lithium Metal Anode: Influence on Charge Transfer Resistance and Short Circuit Prevention. *Journal of The Electrochemical Society* **2017,** *164* (4), A666.
27. Barai, P.; Higa, K.; Ngo, A. T.; Curtiss, L. A.; Srinivasan, V., Mechanical Stress Induced Current Focusing and Fracture in Grain Boundaries. *Journal of The Electrochemical Society* **2019,** *166* (10), A1752.
28. Barai, P.; Ngo, A. T.; Narayanan, B.; Higa, K.; Curtiss, L. A.; Srinivasan, V., The Role of Local Inhomogeneities on Dendrite Growth in Llzo-Based Solid Electrolytes. *Journal of the Electrochemical Society* **2020,** *167* (10), 100537.
29. Porz, L.; Swamy, T.; Sheldon, B. W.; Rettenwander, D.; Frömling, T.; Thaman, H. L.; Berendts, S.; Uecker, R.; Carter, W. C.; Chiang, Y. M., Mechanism of Lithium Metal Penetration through Inorganic Solid Electrolytes. *Advanced Energy Materials* **2017,** *7* (20), 1701003.
30. Vishnugopi, B. S.; Dixit, M. B.; Hao, F.; Shyam, B.; Cook, J. B.; Hatzell, K. B.; Mukherjee, P. P., Mesoscale Interrogation Reveals Mechanistic Origins of Lithium Filaments Along Grain Boundaries in Inorganic Solid Electrolytes. *Advanced Energy Materials* **2022,** *12* (3), 2102825.
31. Shen, F.; Dixit, M. B.; Xiao, X.; Hatzell, K. B., Effect of Pore Connectivity on Li Dendrite Propagation within Llzo Electrolytes Observed with Synchrotron X-Ray Tomography. *ACS Energy Letters* **2018,** *3* (4), 1056-1061.

32. Swamy, T.; Park, R.; Sheldon, B. W.; Rettenwander, D.; Porz, L.; Berendts, S.; Uecker, R.; Carter, W. C.; Chiang, Y.-M., Lithium Metal Penetration Induced by Electrodeposition through Solid Electrolytes: Example in Single-Crystal Li6la3zrtao12 Garnet. *Journal of The Electrochemical Society* **2018,** *165* (16), A3648.
33. Liu, X.; Garcia-Mendez, R.; Lupini, A. R.; Cheng, Y.; Hood, Z. D.; Han, F.; Sharafi, A.; Idrobo, J. C.; Dudney, N. J.; Wang, C., Local Electronic Structure Variation Resulting in Li 'Filament'formation within Solid Electrolytes. *Nature Materials* **2021,** *20* (11), 1485-1490.
34. Han, F.; Westover, A. S.; Yue, J.; Fan, X.; Wang, F.; Chi, M.; Leonard, D. N.; Dudney, N. J.; Wang, H.; Wang, C., High Electronic Conductivity as the Origin of Lithium Dendrite Formation within Solid Electrolytes. *Nature Energy* **2019,** *4* (3), 187-196.
35. Monroe, C.; Newman, J., The Impact of Elastic Deformation on Deposition Kinetics at Lithium/Polymer Interfaces. *Journal of The Electrochemical Society* **2005,** *152* (2), A396.
36. Monroe, C.; Newman, J., The Effect of Interfacial Deformation on Electrodeposition Kinetics. *Journal of The Electrochemical Society* **2004,** *151* (6), A880.
37. Mistry, A.; Mukherjee, P. P., Molar Volume Mismatch: A Malefactor for Irregular Metallic Electrodeposition with Solid Electrolytes. *Journal of the Electrochemical Society* **2020,** *167* (8), 082510.
38. Wang, M.; Wolfenstine, J. B.; Sakamoto, J., Temperature Dependent Flux Balance of the Li/Li7la3zr2o12 Interface. *Electrochimica Acta* **2019,** *296*, 842-847.
39. Krauskopf, T.; Mogwitz, B.; Rosenbach, C.; Zeier, W. G.; Janek, J., Diffusion Limitation of Lithium Metal and Li–Mg Alloy Anodes on Llzo Type Solid Electrolytes as a Function of Temperature and Pressure. *Advanced Energy Materials* **2019,** *9* (44), 1902568.
40. Kasemchainan, J.; Zekoll, S.; Spencer Jolly, D.; Ning, Z.; Hartley, G. O.; Marrow, J.; Bruce, P. G., Critical Stripping Current Leads to Dendrite Formation on Plating in Lithium Anode Solid Electrolyte Cells. *Nature materials* **2019,** *18* (10), 1105-1111.
41. Wang, M. J.; Choudhury, R.; Sakamoto, J., Characterizing the Li-Solid-Electrolyte Interface Dynamics as a Function of Stack Pressure and Current Density. *Joule* **2019,** *3* (9), 2165-2178.
42. Kazyak, E.; Garcia-Mendez, R.; LePage, W. S.; Sharafi, A.; Davis, A. L.; Sanchez, A. J.; Chen, K.-H.; Haslam, C.; Sakamoto, J.; Dasgupta, N. P., Li Penetration in Ceramic Solid Electrolytes: Operando Microscopy Analysis of Morphology, Propagation, and Reversibility. *Matter* **2020,** *2* (4), 1025-1048.
43. Dixit, M. B.; Verma, A.; Zaman, W.; Zhong, X.; Kenesei, P.; Park, J. S.; Almer, J.; Mukherjee, P. P.; Hatzell, K. B., Synchrotron Imaging of Pore Formation in Li Metal Solid-State Batteries Aided by Machine Learning. *ACS Applied Energy Materials* **2020,** *3* (10), 9534-9542.
44. Lewis, J. A.; Cortes, F. J. Q.; Liu, Y.; Miers, J. C.; Verma, A.; Vishnugopi, B. S.; Tippens, J.; Prakash, D.; Marchese, T. S.; Han, S. Y., Linking Void and Interphase Evolution to Electrochemistry in Solid-State Batteries Using Operando X-Ray Tomography. *Nature Materials* **2021,** *20* (4), 503-510.
45. Dixit, M.; Parejiya, A.; Essehli, R.; Muralidharan, N.; Haq, S. U.; Amin, R.; Belharouak, I., Solidpac Is an Interactive Battery-on-Demand Energy Density Estimator for Solid-State Batteries. *Cell Reports Physical Science* **2022,** *3* (2), 100756.
46. Bielefeld, A.; Weber, D. A.; Janek, J. r., Modeling Effective Ionic Conductivity and Binder Influence in Composite Cathodes for All-Solid-State Batteries. *ACS applied materials & interfaces* **2020,** *12* (11), 12821-12833.
47. Bielefeld, A.; Weber, D. A.; Janek, J. r., Microstructural Modeling of Composite Cathodes for All-Solid-State Batteries. *The journal of physical chemistry C* **2018,** *123* (3), 1626-1634.
48. Naik, K. G.; Vishnugopi, B. S.; Mukherjee, P. P., Kinetics or Transport: Whither Goes the Solid-State Battery Cathode? *ACS Applied Materials & Interfaces* **2022** (https://doi.org/10.1021/acsami.2c04962).
49. Nam, Y. J.; Oh, D. Y.; Jung, S. H.; Jung, Y. S., Toward Practical All-Solid-State Lithium-Ion Batteries with High Energy Density and Safety: Comparative Study for Electrodes Fabricated by Dry-and Slurry-Mixing Processes. *Journal of Power Sources* **2018,** *375*, 93-101.

50. Shi, T.; Tu, Q.; Tian, Y.; Xiao, Y.; Miara, L. J.; Kononova, O.; Ceder, G., High Active Material Loading in All-Solid-State Battery Electrode Via Particle Size Optimization. *Advanced Energy Materials* **2020,** *10* (1), 1902881.
51. Strauss, F.; Bartsch, T.; de Biasi, L.; Kim, A.-Y.; Janek, J. r.; Hartmann, P.; Brezesinski, T., Impact of Cathode Material Particle Size on the Capacity of Bulk-Type All-Solid-State Batteries. *ACS Energy Letters* **2018,** *3* (4), 992-996.
52. Davis, A. L.; Goel, V.; Liao, D. W.; Main, M. N.; Kazyak, E.; Lee, J.; Thornton, K.; Dasgupta, N. P., Rate Limitations in Composite Solid-State Battery Electrodes: Revealing Heterogeneity with Operando Microscopy. *ACS Energy Letters* **2021,** *6* (8), 2993-3003.
53. Minnmann, P.; Quillman, L.; Burkhardt, S.; Richter, F. H.; Janek, J., Editors' Choice—Quantifying the Impact of Charge Transport Bottlenecks in Composite Cathodes of All-Solid-State Batteries. *Journal of The Electrochemical Society* **2021,** *168* (4), 040537.
54. Balaish, M.; Gonzalez-Rosillo, J. C.; Kim, K. J.; Zhu, Y.; Hood, Z. D.; Rupp, J. L., Processing Thin but Robust Electrolytes for Solid-State Batteries. *Nature Energy* **2021,** *6* (3), 227-239.
55. Mistry, A.; Usseglio-Viretta, F. L.; Colclasure, A.; Smith, K.; Mukherjee, P. P., Fingerprinting Redox Heterogeneity in Electrodes During Extreme Fast Charging. *Journal of The Electrochemical Society* **2020,** *167* (9), 090542.
56. Vishnugopi, B. S.; Verma, A.; Mukherjee, P. P., Fast Charging of Lithium-Ion Batteries Via Electrode Engineering. *Journal of The Electrochemical Society* **2020,** *167* (9), 090508.
57. Graingeo Handbook, in Geodict 2022 User Guide from Math2market Gmbh, Germany. doi.org/10.30423/userguide.geodict2022.
58. Stöffler, H.; Zinkevich, T.; Yavuz, M.; Senyshyn, A.; Kulisch, J. r.; Hartmann, P.; Adermann, T.; Randau, S.; Richter, F. H.; Janek, J. r., Li+-Ion Dynamics in B-Li3ps4 Observed by Nmr: Local Hopping and Long-Range Transport. *The Journal of Physical Chemistry C* **2018,** *122* (28), 15954-15965.
59. Homma, K.; Yonemura, M.; Kobayashi, T.; Nagao, M.; Hirayama, M.; Kanno, R., Crystal Structure and Phase Transitions of the Lithium Ionic Conductor Li3ps4. *Solid State Ionics* **2011,** *182* (1), 53-58.
60. Liu, Z.; Fu, W.; Payzant, E. A.; Yu, X.; Wu, Z.; Dudney, N. J.; Kiggans, J.; Hong, K.; Rondinone, A. J.; Liang, C., Anomalous High Ionic Conductivity of Nanoporous B-Li3ps4. *Journal of the American Chemical Society* **2013,** *135* (3), 975-978.
61. Zahiri, B.; Patra, A.; Kiggins, C.; Yong, A. X. B.; Ertekin, E.; Cook, J. B.; Braun, P. V., Revealing the Role of the Cathode–Electrolyte Interface on Solid-State Batteries. *Nature Materials* **2021,** *20* (10), 1392-1400.
62. Pervez, S. A.; Kim, G.; Vinayan, B. P.; Cambaz, M. A.; Kuenzel, M.; Hekmatfar, M.; Fichtner, M.; Passerini, S., Overcoming the Interfacial Limitations Imposed by the Solid–Solid Interface in Solid-State Batteries Using Ionic Liquid-Based Interlayers. *Small* **2020,** *16* (14), 2000279.
63. Guo, F.; Wu, C.; Chen, H.; Zhong, F.; Ai, X.; Yang, H.; Qian, J., Dendrite-Free Lithium Deposition by Coating a Lithiophilic Heterogeneous Metal Layer on Lithium Metal Anode. *Energy Storage Materials* **2020,** *24*, 635-643.

Table of Contents Graphic

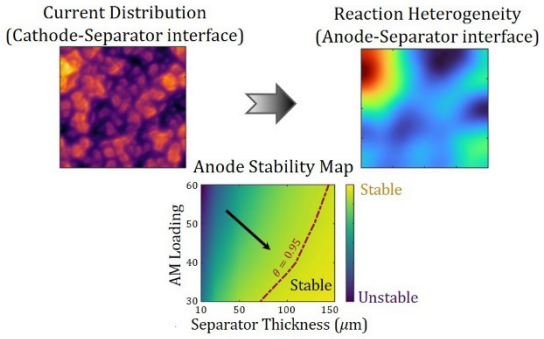

Supporting Information

Solid Electrolyte-Cathode Interface Dictates Reaction Heterogeneity and Anode Stability

Kaustubh G. Naik,[#] Debanjali Chatterjee,[#] and Partha P. Mukherjee[*]

School of Mechanical Engineering, Purdue University, West Lafayette, IN 47907, USA

[#]Contributed equally to this work.

[*]*Correspondence*: pmukherjee@purdue.edu

Table S1. List of properties and parameters used in the modeling framework[1, 2].

Parameters		**Values**	**Units**
k_0	Intrinsic ionic conductivity of SE (β-Li_3PS_4)	0.0093 (at 20°C)	S m^{-1}
i_0	Anode exchange current density	2	mA cm^{-2}
T	Operating temperature	293.15 (Unless specified otherwise)	K
T_{ref}	Reference temperature	293.15	K
$E_{a,\kappa}$	Activation energy for ionic transport	34.7	kJ mol^{-1}
V_{cell}	Operating cell voltage	3.65	V
C_0	Nominal capacity of NMC622	180	mAh g^{-1}
ρ_{AM}	Density of NMC622	4.65	g cm^{-3}
ρ_{SE}	Density of β-Li_3PS_4 SE	1.87	g cm^{-3}
ρ_{CBD}	Density of PVDF/C (CBD)	1.78	g cm^{-3}
ρ_a	Density of Li anode	0.54	g cm^{-3}
ρ_{Al}	Density of aluminum	2.7	g cm^{-3}
ρ_{cu}	Density of copper	8.96	g cm^{-3}
a_{total}	Cross-sectional area	200×200	μm^2
i_{app}	Applied current density	5 (Unless specified otherwise)	mA cm^{-2}
L_c	Cathode thickness	70	µm

L_a	Li-metal anode thickness	30	µm
L_{Al}	Aluminum current collector thickness	10	µm
L_{Cu}	Copper current collector thickness	5	µm

S1. Temperature Dependent Ionic Conductivity of β-Li_3PS_4 Solid Electrolyte (SE)

Ionic conductivity of β-Li_3PS_4 SE is strongly dependent on temperature, thus influencing the ionic transport in the SE separator. As a result, temperature plays a vital role in the propagation of the heterogeneous current distribution from the cathode-separator interface to the anode-separator interface. To incorporate the temperature dependent ionic conductivity in the model, Arrhenius equation is adopted as expressed in Eq. (6) of the main manuscript. Recently, Stöffler *et al.* [1] investigated the long-range Li^+ transport in β-Li_3PS_4 SE using impedance spectroscopy. The Arrhenius plot obtained by Stöffler *et al.*[1] is recreated and plotted in Figure S1. From the plot presented in Figure S1, the ionic conductivity at the reference temperature (20 °C) is estimated to be 0.0093 S/m and the activation energy 0.36 eV (same as 34.7 kJ/mol).

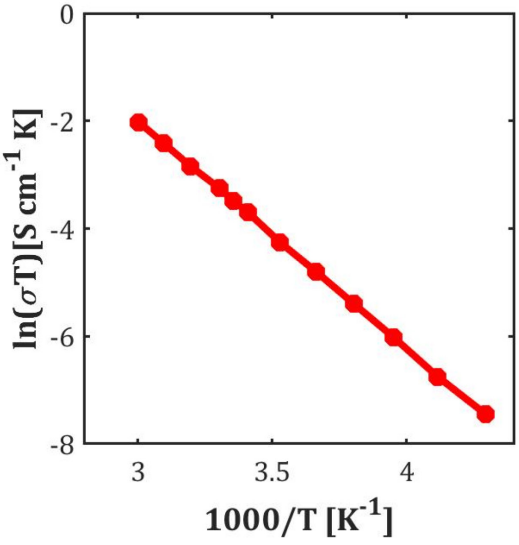

Figure S1. Arrhenius plot for ionic conductivity of β-Li_3PS_4 SE obtained from Stöffler *et al.*[1]

S2. Quantifying Current Distribution at the Cathode-Separator Interface

Current distribution at the cathode-separator interface acts as a boundary condition for the ionic transport in the SE separator. To obtain the current distribution at the cathode-separator interface, a macro-homogeneous solid-state battery (SSB) model is used, which has been developed in our previous study[3] to study the reaction kinetics and transport limitations in the solid-state battery cathode. Here, we simultaneously solve for the Butler-Volmer kinetics at the AM-SE interface, ionic transport through the SE phase, electron transport through the AM-CBD phase and solid-state lithium diffusion through the spherical AM particles. The corresponding mathematical equations are as follows:

Butler-Volmer Kinetics at the AM-SE interface:

$$i = i_0 \left[\exp\left(\frac{F}{2RT}\eta\right) - \exp\left(\frac{-F}{2RT}\eta\right)\right] \tag{S1}$$

Solid-state lithium diffusion:

$$\frac{\partial c_s}{\partial t} = \frac{1}{r^2}\frac{\partial}{\partial r}\left(D_s r^2 \frac{\partial c_s}{\partial r}\right) \tag{S2}$$

Ionic transport in SE phase:

$$\nabla \cdot (\kappa^{eff} \nabla \phi_{SE}) + j = 0 \tag{S3}$$

Electron transport in AM phase:

$$\nabla . (\sigma^{eff} \nabla \phi_{AM}) - j = 0 \tag{S4}$$

Here, i_0 is the exchange current density, η is the overpotential, c_s is the lithium concentration in AM particle, D_s is the lithium diffusivity, ϕ_{SE} is the potential in SE phase of composite cathode, ϕ_{AM} is the potential in AM phase of the composite cathode, and j is the volumetric current density. During charging, electrochemical reactions occur at the AM-SE interfaces within the composite cathode and the lithium ions generated are subsequently transported through the SE phase. Hence, current corresponding to all the electrochemical reactions occurring in the bulk of the cathode is carried by the SE phase at the cathode-separator interface (see Figure S2). The AM phase at the cathode-separator interface only contributes to the current arising from the electrochemical reactions occurring at the cathode-separator interface (as shown in Figure S2). The modeling domain used for the macro-homogeneous model for the composite cathode is also shown in Figure S2. Based on the model output, reaction current and the ionic current can be quantified at each node of the computational domain. As a result, the reaction current obtained at the rightmost node (contributed by the AM phase) shown in Figure S2 can be taken as the current arising from the electrochemical reactions at the cathode-separator interface. On the other hand, rest of the current is contributed by the ionic current in the SE phase at the cathode-separator interface. In this way, specific to the cathode-separator interface, distinction between the currents contributed by the SE phase and the AM phase is established which helps us to quantify the current heterogeneity at the cathode-separator interface. Evolution of these two currents has been plotted in Figure 1(c) of the main manuscript, where it is observed that almost all the current is contributed by the SE phase at the cathode-separator interface. Importantly, contribution from the AM phase becomes almost zero towards the end of the charging process. From this observation, it can be inferred that all the AM present at the cathode-separator interface gets delithiated towards the end of the charging process. Thus, the current heterogeneity is maximum towards the end of the charging process. In this way,

the current distribution at the cathode-separator interface is evaluated and used as the boundary condition for the ion transport through the SE separator to study the reaction heterogeneity at the anode-SE interface.

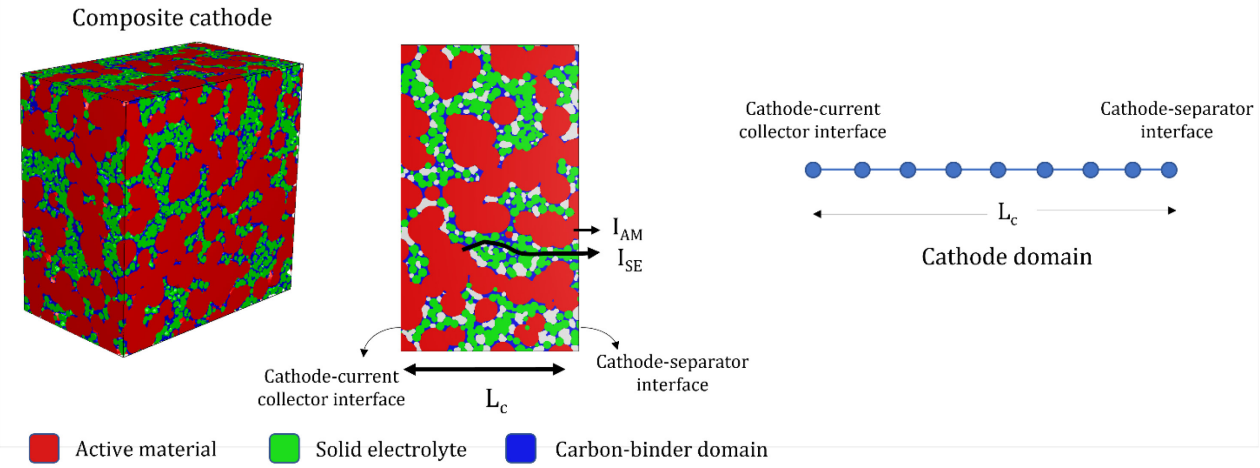

Figure S2. Schematic of a solid-state cathode, 2D cross-section showing the difference between I_{AM} and I_{SE}, and the corresponding computational domain.

S3. Reaction Heterogeneity Analysis for High Active Material Loading Cathode (80 vol. % AM)

As solid-state batteries should be pushing towards higher AM loading (~ 80 vol. % AM) to increase the energy density, in this section, reaction heterogeneity at the anode-separator interface has been analyzed for the composite cathode with high AM loading (80 vol. % AM, 15 vol. % SE, 5 vol. % CBD + voids). Figure S3(a) shows the material map and current distribution at the cathode-separator interface, and the reaction heterogeneity at the anode-separator interface for the separator thickness of 40 μm. As discussed in the main manuscript, the locations with SE phase at the cathode-separator interface experience severe current focusing which leads to the reaction heterogeneity at the anode-separator interface as shown in Figure S3(a). Figure S3(b) shows this reaction heterogeneity as a function of separator thickness. When compared to the reaction

heterogeneity trends shown in Figure 5(b) of the main manuscript, it is evident that the reaction heterogeneity at the anode-separator interface is severe for high AM loading composite cathode. Thus, to enable stable operation of high energy density SSB, in addition to addressing the ion transport limitations (due to higher tortuosities), cathode microstructure induced reaction heterogeneity at the anode-separator interface should also be addressed. In addition, critical separator thickness, L_c, where the electrochemical reactions at the anode-separator interface become almost homogeneous ($\frac{i_{max}-i_{min}}{i_{app}} = 0.05$) for the high AM loading case considered here is almost 200 μm. Thus, achieving homogeneous electrodeposition will come at the cost of energy density. Hence, strategies such as the architected cathode discussed in the main manuscript should be helpful in achieving stable high energy density SSBs.

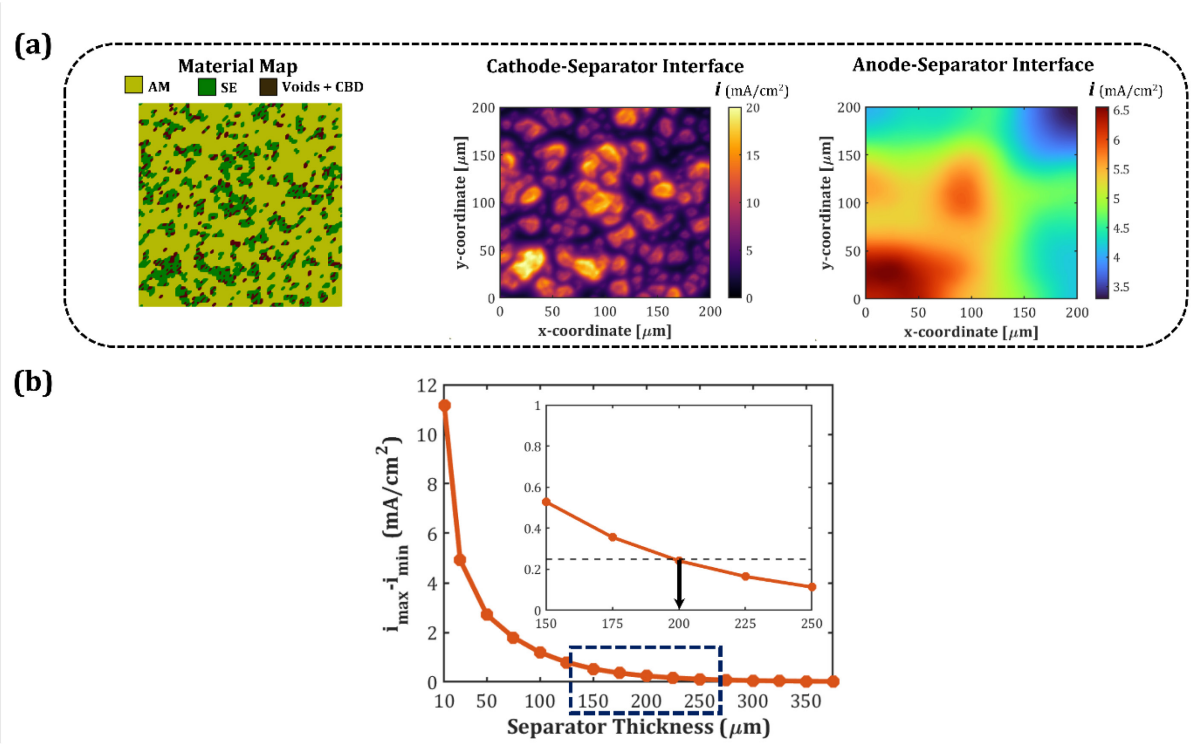

Figure S3. (a) Material map of the cathode-separator interface followed by current distribution and reaction heterogeneity at the cathode-separator and the anode-separator interfaces, respectively, for applied current density of 5 mA/cm^2 and separator thickness of 40 μm. (b)

Reaction heterogeneity ($i_{max} - i_{min}$) as a function of the separator thickness for the composite cathode considered in (a).

S4. Dynamic Evolution of the Heterogeneities at the Electrode-Separator Interfaces

In this section, we analyze the dynamic evolution of the heterogeneities at the cathode-separator and anode-separator interfaces for cathode composition of 60 vol. % AM, 20 vol. % SE and 20 vol. % CBD and voids with applied current density of 5 mA/cm^2. Figure 1(c) of the main manuscript has been shown in Figure S4(a) which depicts the dynamic evolution of the current contributed by the regions having AM and SE phases at the cathode-separator interface. From Figure S4(a), it is evident that most of the current at the cathode-separator interface is carried by the regions having SE phase. This result has been explained in detail in Section S2. It is noted that the contribution from the regions with AM phase gradually fades over the cell operation and become almost negligible towards the end of the charging process. This is attributed to the complete delithiation of the AM phase present at the cathode-separator interface. Figure S4(b) represents the material map of the cathode-separator interface showing the distribution of the constituent phases. Figure S4(d) and Figure S4(e) shows the heterogeneities at the two interfaces for four time instances as indicated by the markers in Figure S4(a). From the heterogeneity maps, it is observed that there is a negligible variation in the heterogeneities over the charging process. The dynamic evolution of the reaction heterogeneity at the anode-separator interface, quantified by ($i_{max} - i_{min}$) is shown in Figure S4(c). Reaction heterogeneity is observed to be almost constant during the charging process (showing a very slight increase from 1.9 mA/cm^2 at the start to 2.3 mA/cm^2 at the end of charge as seen in Figure S4(c)). For this reason, it is reasonable to approximate that all the current at the cathode-separator interface is contributed by the regions

having SE phase. This also allows us to account for the most severe heterogeneities seen at the interfaces during the charging process.

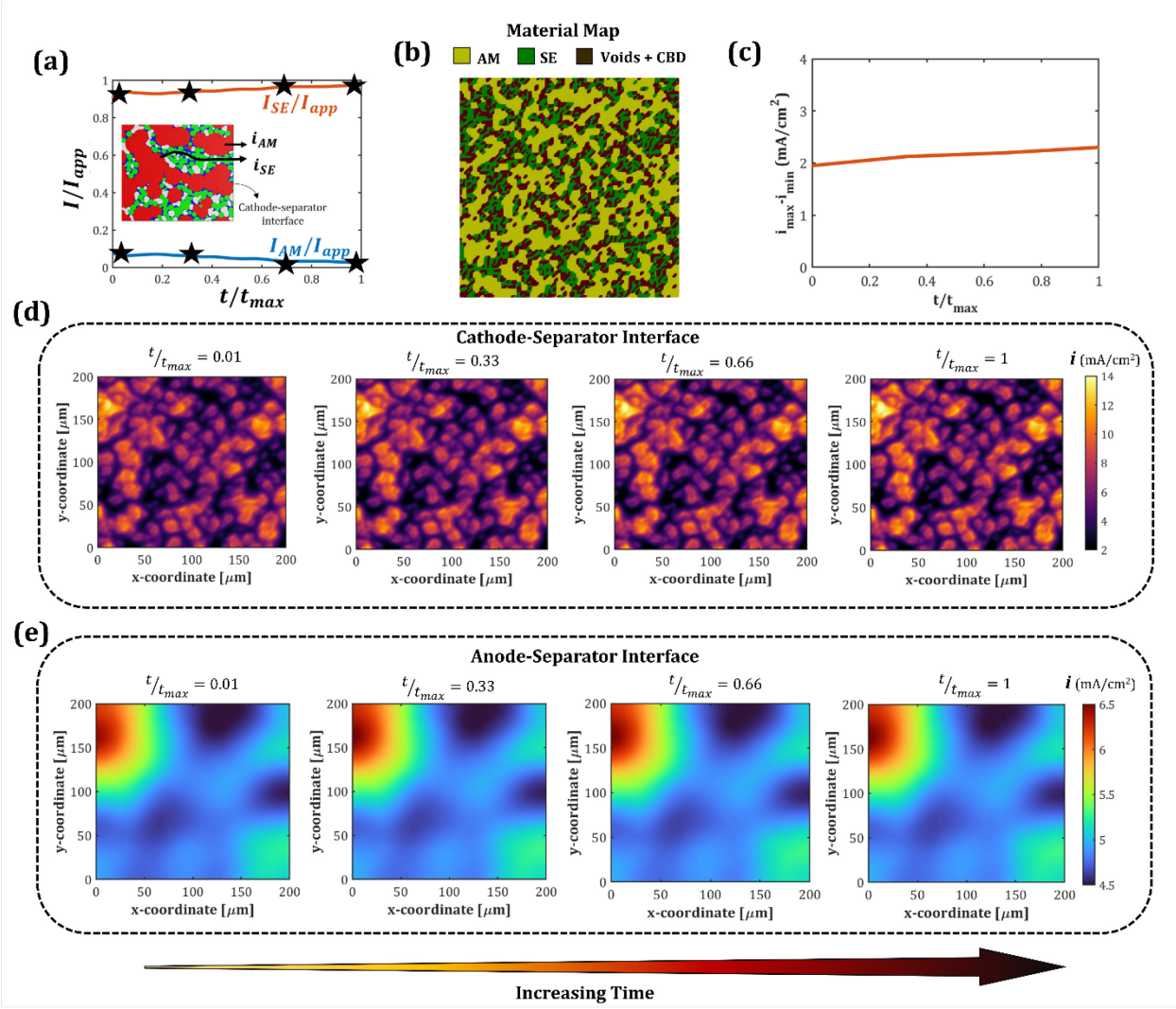

Figure S4. (a) Fraction of the total current contributed by the regions with AM phase and the regions with SE phase at the cathode-separator interface as a function of time for the applied current of 5 mA/cm^2 and cathode composition of 60 vol. % AM, 20 vol. % SE and 20 vol. % CBD and voids. (b) Material map for the cathode-separator interface considered. (c) Dynamic evolution of the reaction heterogeneity ($i_{max} - i_{min}$) at the anode-separator interface. (d) Current distribution at the cathode-separator interface at four time instances as indicated by markers in (a). (e) Reaction distribution at the anode-separator interface corresponding to the instances shown in (d).

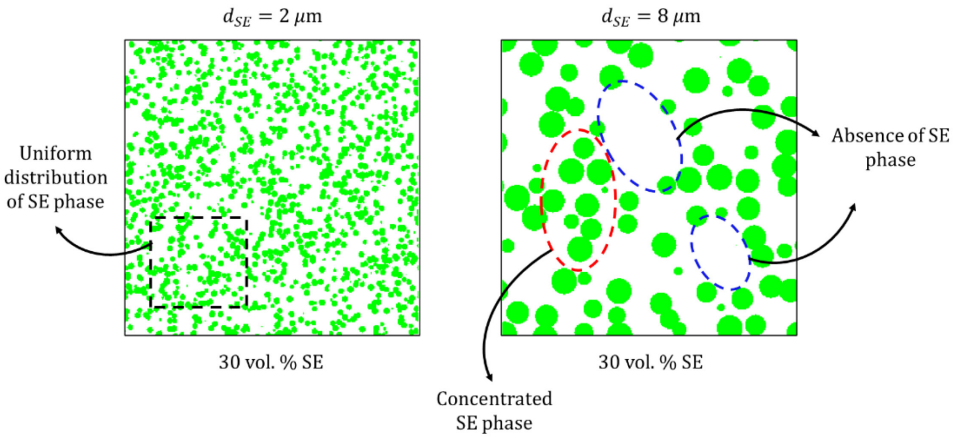

Figure S5. Spatial variability of the SE phase for smaller and larger SE particles. Larger SE particles occupy larger chunks of space on the cathode-separator interface, simultaneously forming large chunks of space where the SE phase is absent, resulting in current focusing. On the other hand, smaller SE particles can be more uniformly distributed, resulting in relatively uniform current distribution at the interface.

References:

1. Stöffler, H.; Zinkevich, T.; Yavuz, M.; Senyshyn, A.; Kulisch, J. r.; Hartmann, P.; Adermann, T.; Randau, S.; Richter, F. H.; Janek, J. r., Li+-Ion Dynamics in B-Li3ps4 Observed by Nmr: Local Hopping and Long-Range Transport. *The Journal of Physical Chemistry C* **2018,** *122* (28), 15954-15965.
2. Dixit, M. B.; Parejiya, A.; Muralidharan, N.; Essehli, R.; Amin, R.; Belharouak, I., Understanding Implications of Cathode Architecture on Energy Density of Solid-State Batteries. *Energy Storage Materials* **2021,** *40*, 239-249.
3. Naik, K. G.; Vishnugopi, B. S.; Mukherjee, P. P., Kinetics or Transport: Whither Goes the Solid-State Battery Cathode? *ACS Applied Materials & Interfaces* **2022** (https://doi.org/10.1021/acsami.2c04962).